Received: 29 March 2022 | Revised: 30 May 2022 | Accepted: 10 June 2022

DOI: 10.1002/appl.202200024

REVIEW

Recent developments in phase-change memory

Andrea Ehrmann[1] | **Tomasz Blachowicz**[2] | **Guido Ehrmann**[3] | **Thomas Grethe**[4]

[1]Faculty of Engineering and Mathematics, Bielefeld University of Applied Sciences, Bielefeld, Germany

[2]Institute of Physics, Center for Science and Education, Silesian University of Technology, Gliwice, Poland

[3]Virtual Institute of Applied Research on Advanced Materials (VIARAM)

[4]Faculty of Textile and Clothing Technology, Niederrhein University of Applied Sciences, Mönchengladbach, Germany

Correspondence
Andrea Ehrmann, Faculty of Engineering and Mathematics, Bielefeld University of Applied Sciences, Bielefeld, Germany.
Email: andrea.ehrmann@fh-bielefeld.de

Abstract

Phase-change memory (PCM) belongs to the nonvolatile solid-state memory techniques. Usually, a chalcogenide is sandwiched between two conductive electrodes and data are stored by setting each cell to a low-resistance (crystalline) or a high-resistance (amorphous) state. Switching between these states is relatively fast, which makes phase-change random access memories (PCRAMs) highly interesting for nonvolatile memories. Multilevel cells, which can store more than 1 bit per cell, and multilayer high-density memory arrays have also been reported as advantages of PCRAM. Writing currents and data retention, on the other hand, still show potential for optimization. This review gives an overview of the most recent developments in new material compositions and material-related optimization of PCM in comparison with already produced PCM.

KEYWORDS

chalcogenides, nonvolatile memory, phase change material, phase-change memory

INTRODUCTION

The physical basics of phase change memories (PCMs), that is, the possibility to change between states of significantly different resistance upon changing between crystalline and amorphous phases of a phase change material, were first reported more than 50 years ago [1]. Many research attempts were reported since, usually based on semiconducting chalcogenide glasses. Such chalcogenide glasses contain the chemical elements sulfur, selenium, and tellurium of Group 16, alloyed with Group 15 elements such as arsenic or antimony, or Group 14 elements such as germanium or tin [2]. The glasses can be doped with rare-earth elements and show interesting optical properties, such as a high degree of nonlinearity and photoinduced effects [2]. For optical storage media such as rewritable digital versatile disks (DVDs) and Blu-ray Disc, GeSbTe systems are used [3,4]. The effect is based on switching a material between amorphous and crystalline phase by SET and RESET pulses, as depicted in Figure 1.

Applying chalcogenides as PCMs necessitates sandwiching them between metal electrodes and measuring the resistance across the chalcogenide. In these applications, often $Ge_2Sb_2Te_5$ is used, whereas nitrogen-doped $Ge_2Sb_2Te_5$ as well as pure and Ag- or In-doped Sb_2Te and some other materials are also investigated [6]. Improving PCMs is based on a combination of optimized—often very small—dimensions and materials. Both parameters influence physical properties such as crystallization and melting temperature, electric and thermal conductivity of both phases, speed of crystallization, and so on, and thus cannot be treated completely independently.

Here we focus on the most recent developments in materials sciences, taking into account the correlated dimensions of the systems. The review is structured as follows: Firstly, the alloys recently suggested for PCMs are described. Next, the latest progress in developing these chalcogenides further or investigating new alloys is illustrated. Then, multilevel-cell memory approaches with more than 1 bit per cell are described. Subsequently, new ideas to use

This is an open access article under the terms of the Creative Commons Attribution License, which permits use, distribution and reproduction in any medium, provided the original work is properly cited.
© 2022 The Authors. *Applied Research* published by Wiley-VCH GmbH.

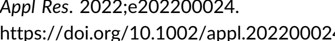

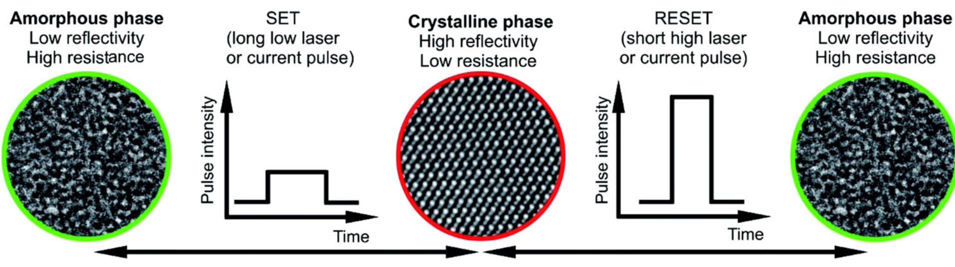

FIGURE 1 Operation principle of phase change memories (PCMs), with the structural material phase defining the logical state of a PCM cell. Typically, the crystalline phase is equal to State 1, whereas the amorphous phase is regarded as State 0. From Lotnyk et al.,[5] originally published under a CC-BY license.

PCMs as part of non-von Neumann computers are depicted. Finally, commercial PCMs are depicted from their first announcement in 2008.

$GE_2SB_2TE_5$ AS A TYPICAL PCM MATERIAL

Recently, the most often investigated alloy used for PCMs is $Ge_2Sb_2Te_5$, with some other structures from these components also reported in the literature. Figure 2 depicts structures of $Ge_2Sb_2Te_5$ (Figure 2e) and other possible alloys from these materials [7]. It should be mentioned that the metastable rock-salt-like cubic structure depicted in Figure 2d–f show ordered vacancies, opposite to structures used for memory switching with disordered vacancies [7]. Generally, $Ge_2Sb_2Te_5$ as the most often used material can be switched between a stable hexagonal phase (Figure 2b), a metastable face centered cubic (fcc) phase (similar to Figure 2e), and an amorphous phase, with varying band gaps and other physical properties [8]. Data recording is performed by reversibly switching between amorphous and crystalline phase [8], as firstly mentioned by Yamada et al. [9] and recently described in more detail [10,11]. GeTe and Sb_2Te_3 are both octahedral structures and show similar electronic properties; therefore, they mix well and $Ge_2Sb_2Te_5$ can be understood as a pseudo binary alloy of these two compounds. This mixture shows a higher thermal stability than each component alone, which renders it especially interesting for PCM materials [12].

In the typical $Ge_2Sb_2Te_5$ fcc rock salt structure, Te forms a perfect octahedral sublattice, whereas Ge, Sb, and vacancies form the other octahedral sublattice, which is disordered. Generally, all Ge/Sb/Te alloys used for PCMs have a metastable rock salt structure with vacancies [13], which transforms into a hexagonal structure upon heating. In these alloys, strong bonds are formed due to the high similarity of their valence orbitals and vacancies usually occur near to the Te atoms, so that the disorder of the Ge/Sb/vacancy sublattice has a certain structure [13]. Although these basic ideas of the material are understood, other questions related to its physico-chemical properties remain open, suggesting more simulations. Mocanu et al. [14] suggested a machine-learning-based interatomic potential enabling large-scale simulation of all aggregated states of $Ge_2Sb_2Te_5$, combining high speed with high accuracy, so that a model consisting of 7200 atoms could be used to investigate the medium-range structural order as well as chemical bonding of the atoms. Other research groups concentrated on simulating special processes in $Ge_2Sb_2Te_5$, such as the RESET melting process [15], or on identifying atom chains in the structure [16].

Such $Ge_2Sb_2Te_5$ chalcogenide films can be produced by physical vapor deposition (PVD), which enables tailoring their stoichiometry, whereas atomic layer deposition (ALD) films can be more conformal [17]. Adinolfi et al. [17] used ALD to produce $Ge_2Sb_2Te_5$ PCMs with short write times in the order of 10 ns and a relatively low RESET current density in the order of 10^7 A/cm^2, similar to recent PVD-based PCM devices.

Magnetron sputtering was applied by Lazarenko et al. [18], who prepared $Ge_2Sb_2Te_5$ thin films and studied their optical band gap. They explained the large variety of optical band gap values for amorphous and crystallized films found in the literature for the nominally identical material, not only by the different film thickness, but also on the deposition methods and the annealing temperatures and durations used for crystallization. They also found significant differences of transmission and reflection spectra, depending on the annealing temperature, and showed that these values fitted well to those gained from different literature data. These different optical properties can, for example, be directly used in metal–insulator–metal optical metasurfaces, as shown by Carillo et al. [19] Changing between different colors is depicted in Figure 3, together with the measured reflectance and the necessary metasurface nanostructures [19]. This behavior is explained by the negative value of the permittivity's real part of GeTe in the crystalline phase, that is, a metallic-like optical behavior with resonant absorption in a wavelength range defined by the surface nanostructure, whereas the amorphous phase of GeTe has optical properties similar to a lossy dielectric, so that resonant absorption cannot occur and a flat reflectance spectrum can be expected [19].

Behrens et al. [20] used pulsed laser deposition to produce $Ge_2Sb_2Te_5$ epitaxial and amorphous films, and induced the phase transitions by single laser pulses instead of the normally applied voltage/current pulses. Their experiments revealed different structural transitions, not only between crystalline and amorphous phase,

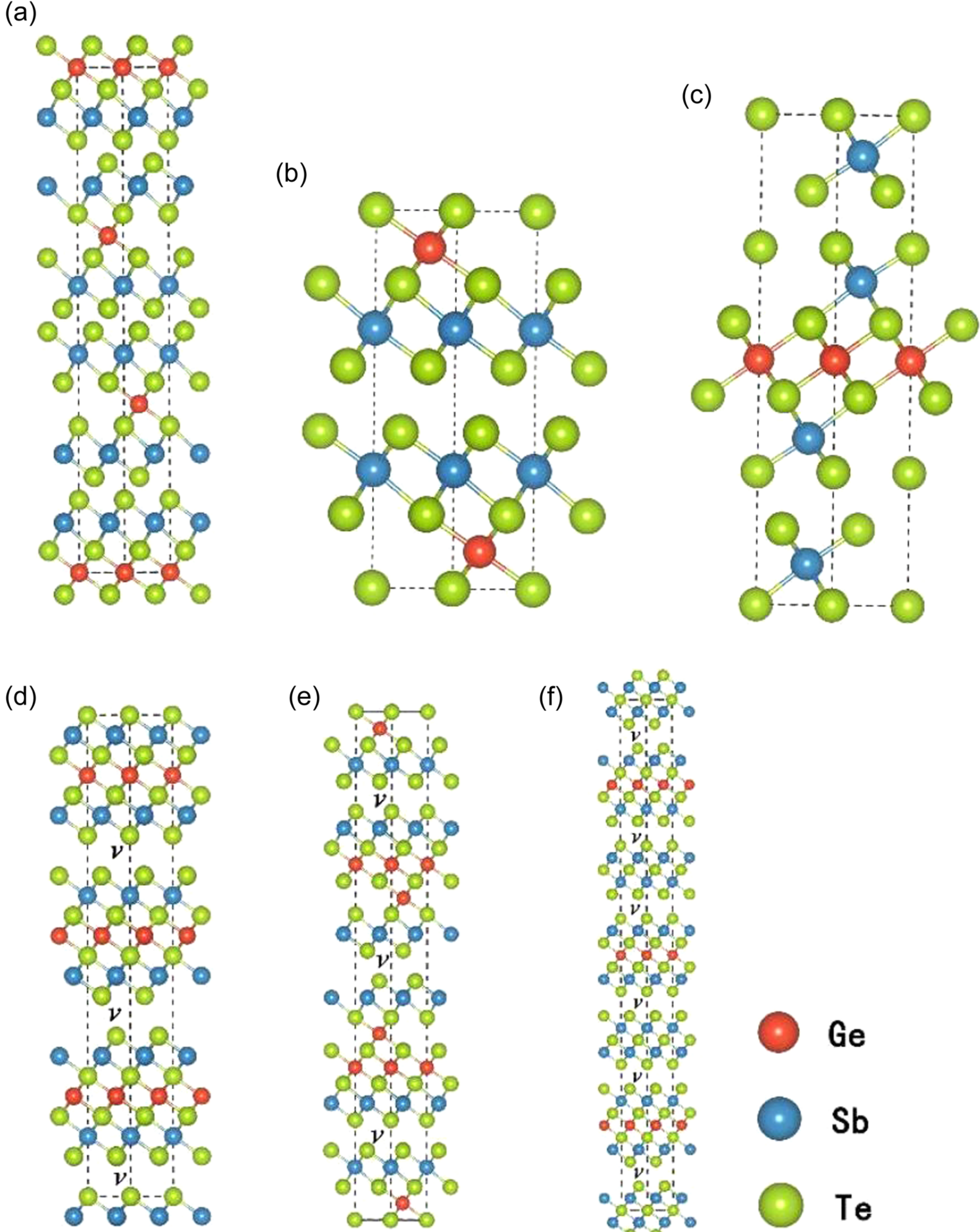

FIGURE 2 Structures for mGeTe•nSb$_2$Te$_3$ phases: (a) stable Ge$_1$Sb$_2$Te$_4$, (b) stable Ge$_2$Sb$_2$Te$_5$, (c) stable Ge$_1$Sb$_4$Te$_7$, (d) metastable Ge$_1$Sb$_2$Te$_4$, (e) metastable Ge$_2$Sb$_2$Te$_5$, (f) metastable Ge$_1$Sb$_4$Te$_7$, *v* represents a vacancy layer. Balls show Ge (red), Sb (blue), and Te (green). From Pan et al. [7], originally published under a CC-BY license.

but also between different crystal phases, with the possibility to tailor the volume ratios of the different phases by the laser flux, that is, to produce multilevel storage systems, as they will be discussed in another section in detail.

A comparison of magnetron-sputtered and thermally deposited Ge$_2$Sb$_2$Te$_5$ thin films was reported by Kozyukhin [21]. In addition, they blended the system with different elements, such as bismuth (Bi), due to its similarity with antimony (Sb) in terms of covalent radii. The chemical bond Bi-Te has lower binding energy than Sb-Te, so that Bi can be expected to replace Sb atoms and to change the type of conduction from *p*-type to *n*-type [22]. Besides, they exchanged Ge by Sn (tin), which has a larger radius than Ge, whereas the Sn-Te bond has a much lower energy than the Ge-Te bond [23]. These experiments showed that addition of bismuth increased the conductivity ratio between the amorphous and the crystalline phase, which is supportive for the use of this material as PCM, whereas addition of Sn significantly reduced the crystallization threshold, in this way enabling rapid crystallization at lower power than in pure Ge$_2$Sb$_2$Te$_5$ [21].

Other authors reported on different doping atoms. Fang et al. [24] reported about Ga$_{0.4}$Ge$_{3.5}$Sb$_{2.3}$Te$_5$, which they produced by cosputtering Ge$_{3.4}$Sb$_{2.3}$Te$_5$ and Ga$_2$Ge$_{3.8}$Sb$_{2.3}$Te$_5$ targets. Compared with the

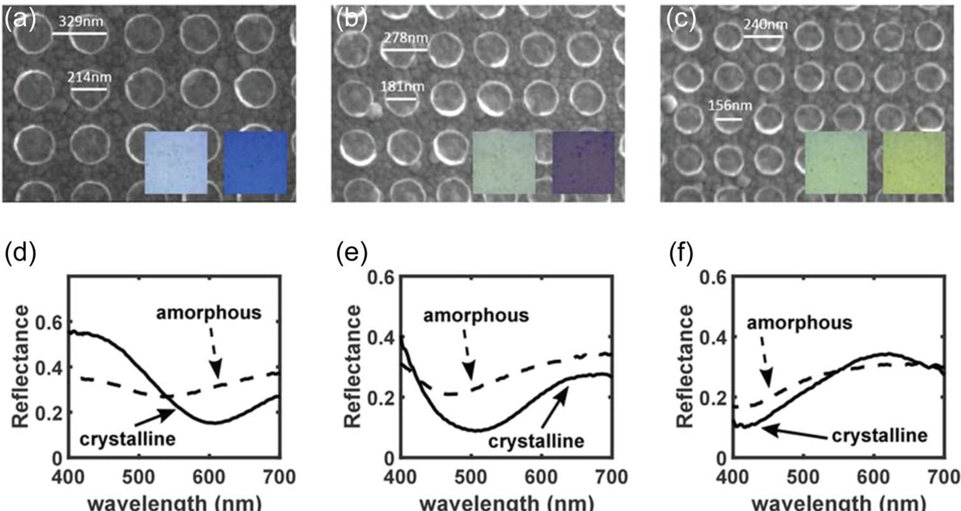

FIGURE 3 Scanning electron microscope (SEM) images of phase-change optical metasurfaces from GeTe for the colors (a) cyan, (b) magenta, and (c) yellow. The optical microscope images in the insets show the colors of the GeTe layer in the amorphous (left) and crystalline (right) states, respectively. (d–f) Measured reflectance spectra for the cyan, magenta, and yellow pixels, respectively. From Carillo et al. [19], originally published under a CC-BY license.

original $Ge_2Sb_2Te_5$, they found a higher crystallization temperature, reduced density change after crystallization, smaller grain size, and lower drift. The electric pulse responsible for the phase change had a duration of only 6 ns and a power consumption of only 0.16 pJ.

Using gadolinium (Gd) as the dopant, Chen et al. [25] showed a higher crystalline resistance and improved thermal stability, combined with reduced grain size. The examination of the crystalline structure revealed that Gd dopants were arbitrarily distributed, with Gd atoms modifying the local structure around the host atoms, and the large coordination number of Gd together with the formation of Gd-Te distorted pentagonal bipyramids was responsible for the high thermal stability.

Doping $Ge_2Sb_2Te_5$ with scandium (Sc), Wang et al. [26] again found a high writing speed of 6 ns, as compared with ~30 ns in common $Ge_2Sb_2Te_5$, in combination with a power consumption of only 23% as compared with the host material. Besides, the 10-year data retention—that is, the maximum temperature allowing to save data for 10 years—was as high as 119°C. These advantages were attributed to the smaller grains and thus reduced stress during crystallization. Their films were magnetron cosputtered from $Ge_2Sb_2Te_5$ and Sc targets, and reached a thickness of 15 nm. Doping $Ge_2Sb_2Te_5$ with Zn resulted even in a 10-year data retention of 167.5°C [27].

Wang et al. [28] used magnetron sputtering to produce the common $Ge_2Sb_2Te_5$ films and $In_{0.9}Ge_2Sb_2Te_5$ films, combined with TiN as the top electrode, to form T-shaped PCM cells. For $In_{0.9}Ge_2Sb_2Te_5$, they found a 10-year retention of 180°C and 6 ns set speed, as well as a reduction of the power consumption of 75%, as compared with the basic $In_{0.9}Ge_2Sb_2Te_5$.

Privitera et al. [29] chose Ge as "dopant" by producing Ge-rich GeSbTe films. The samples were produced by cosputtering $Ge_2Sb_2Te_5$ and a pure Ge target, resulting in $Ge_2Sb_2Te_5$ films with 45 at.% excess Ge and 4 at.% N due to using Ar and N_2 as sputtering gas mixture. The originally amorphous film was crystallized at 400°C, leading to partial segregation of the excess Ge into Ge grains. They found high data retention properties, which they attributed to the long-range diffusion of Ge atoms, responsible for the high crystallization temperature of 275°C for Ge-rich regions and still relatively high 245°C for a reduced amount of excess Ge. Similarly, Ge-rich GeSbTe films were investigated by Kusiak et al. [30] who found a higher phase change temperature and an enhanced thermal resistance. Cecchi et al. [31] investigated the undesired decomposition of such Ge-rich GeSbTe alloys and reported Ge-rich $Ge_2Sb_2Te_5$ to be less susceptible to decomposition than Ge-rich Sb_2Te_3. Applying density functional simulations, El Kheir et al. [32] investigated decomposition of Ge-rich GeSbTe alloys and found several possible decomposition paths without the possibility of regeneration at low temperatures. The opposite approach was chosen by Boniardi et al. [33], who produced $(Ge_2Sb_2Te_5)/Sb_2Te_3$ superlattices, which needed <40% of the SET and RESET currents of common $Ge_2Sb_2Te_5$.

An often used dopant is carbon due to its ability to improve the thermal stability and cycle endurance of the PCM, as compared with pure $Ge_2Sb_2Te_5$. Cheng et al. [34] used transmission electron microscopy (TEM) to investigate the microstructure of C-doped $Ge_2Sb_2Te_5$ and found that C atoms inside the grains increased the cationic migration energy barriers, in this way improving the thermal stability of the metastable FCC phase and suppressing the possible transition into a hexagonal structure, while C atoms around the grains suppressed grain growth. Han et al. [35] found bonding of the excess carbon with Ge and subsequently with Sb in localized regions, which supported the local structures and suppressed undesired stochastic changes, overall leading to a significant improvement of the device stability in the amorphous structure. Li et al. [36] and Song et al. [37] reported a resistance ratio of more than 100 between RESET and SET

states for C-doped $Ge_2Sb_2Te_5$ with a heating bottom electrode contact with nitride coating, enabling programming times of 200 ns and 10-year data retention of 128°C, as well as an endurance of over 10^9 cycles.

Another highly interesting dopant is nitrogen, which is also able to increase the crystallization temperature and reduce the resistivity drift of the RESET state [38]. Luong et al. [38] used nitrogen ion implantation in $Ge_2Sb_2Te_5$ and found a maximum temperature shift of about 50 K for 5% nitrogen. Yu et al. [39] investigated especially the multilevel data storage properties for N-doped $Ge_2Sb_2Te_5$ films and reported about a quasi-platform of resistance due to the improved thermal stability. For Ge-rich GeSbTe alloys, Luong et al. [40] reported slowing down the phase separation, crystallization, and growth during annealing, but also improved stability of the amorphous phase.

As these few examples show, $Ge_2Sb_2Te_5$ offers large potential for improvement by doping with a broad variety of elements, making this alloy in spite of its regular use still highly interesting for new developments. However, there are many other PCM materials that have been investigated in recent years, often containing Ge, Sb, Te, or two of these elements, which will be discussed in the next section.

OTHER RECENT PCM MATERIALS

This section is sorted as follows: Starting with alloys containing Te in combination with Ge and/or Sb, we discuss alloys with Te without Ge or Sb, followed by Ge and Sb alloys without Te, before finally a few possible PCM materials without one of these three typical elements are described.

GeTe alloys

Besides the most often used alloy $Ge_2Sb_2Te_5$, other alloys of Ge, Sb, and Te are described in the literature, such as $Ge_1Sb_2Te_4$. The atomic arrangement of the latter was investigated by Zhu et al. [41] by TEM. They found a stable hexagonal structure with a partially ordered Ge/Sb atomic stacking, different from the fully disordered Ge/Sb arrangement in the metastable rock-salt structure, with a transition between them by opening the van der Waals gap upon Ge/Sb hopping near vacancies. Structural changes of GeSb2Te4 also affect the modification of elastic parameters. These changes were studied by Blachowicz et al. [42] using Brillouin Light Scattering. In the research, elastic constants were determined for the amorphous, cubic fcc, and crystalline hexagonal phases.

Wang et al. [43] investigated Sc-doped GeTe and found very fast operation speed of 6 ns and low power consumption of 7nJ, combined with 10-year data retention of 120°C. The authors attributed the high data retention—very similar to the aforementioned $Ge_2Sb_2Te_5$ doped with Sc [26]—to the high coordination number of Sc and its strong bonds to the Te atoms in the amorphous phase, which weakened the neighboring Ge-Te bonds and thus reduced the melting energy. They reported that in the crystalline phase, Sc atoms were found on Ge vacancies so that a homogeneous rhombohedral phase was formed, as depicted in Figure 4.

Saito et al. [44] used density functional theory simulations to screen diverse PCM materials such as GeTe, the common $Ge_2Sb_2Te_5$, Cu_2GeTe_3, and other Cu-Ge-Te ternary alloys, and found that Cu_2GeTe_3 had the smallest density change between amorphous and crystalline state, which they interpreted as optimum for high-endurance PCM applications.

Ab initio simulations and chemical bonding analyses of amorphous Ge–Sn–Te materials were used to investigate the drift of the electrical resistance, which is known to be reducible by replacing Ge in GeTe partly by Sn [45]. Chen et al. found that optimizing the ratio of Ge to Sn allowed for combining very low resistance drift with fast phase transition, as it is necessary in PCM chips. Other authors reported improvement of the properties of GeTe by oxidation [46] or doping with Bi [47].

Saito et al. [48] used different sputter targets (GeTe and $Ge_{45}Te_{55}$, as well as Sb_2Te_3, $Sb_{33}Te_{67}$, Bi_2Te_3, and $Bi_{30}Te_{70}$) to produce PCM films by radiofrequency sputtering on Si(100) targets at different growth and postannealing temperatures. Their work concentrated on producing highly oriented chalcogenide films and superlattices, investigating the necessary target compositions to reach desired film compositions and optimizing the growth temperature to produce the desired films, while PCM properties were not investigated further.

Besides alloys with a 1:1 ratio of Ge:Te, another often used ratio is 1:3, as mentioned before [46]. Shuang et al. [49] and Shindo et al. [50] found that N-doped $Cr_2Ge_2Te_6$, the alloy suggested theoretically by Saito et al. [48], showed nearly no difference of the electrical resistivity of amorphous and crystalline phases, but nevertheless switching could be measured due to a change of the contact resistance between phase change material and metal electrode of three orders of magnitude.

Other researchers produced multilayers with Ge-Te parts. Li et al. [51] showed that $GaSb/Ge_2Te$ superlattices could be tuned to multilevel resistance states and very high data retention by optimizing the layer thickness ratio, whereas Okabe et al. [52] managed significantly reducing the RESET current in comparison with the common $Ge_2Sb_2Te_5$-based PCM. The latter group investigated the switching mechanism of interfacial PCM, that is, PCM consisting of Sb_2Te_3/GeTe multilayers, more in detail, attributing this RESET current reduction to voids within the multilayers that move to the bottom electrode interface and thus reduce the effective contact area. They suggested improving the layer deposition to receive reliable switching [52].

Finally, it should be mentioned that systematic changes of the material properties occur with changing stoichiometry. For different GeTe allows with GeSe, SnTe, and Sb_2Te_3, Persch et al. [53] described the possibility to design crystallization and vitrification kinetics by tailoring the chemical bonding. In this way, they could modify the minimum crystallization time by several orders of magnitude and also the onset temperature for glass formation, depending on the number of electrons shared and electrons transferred.

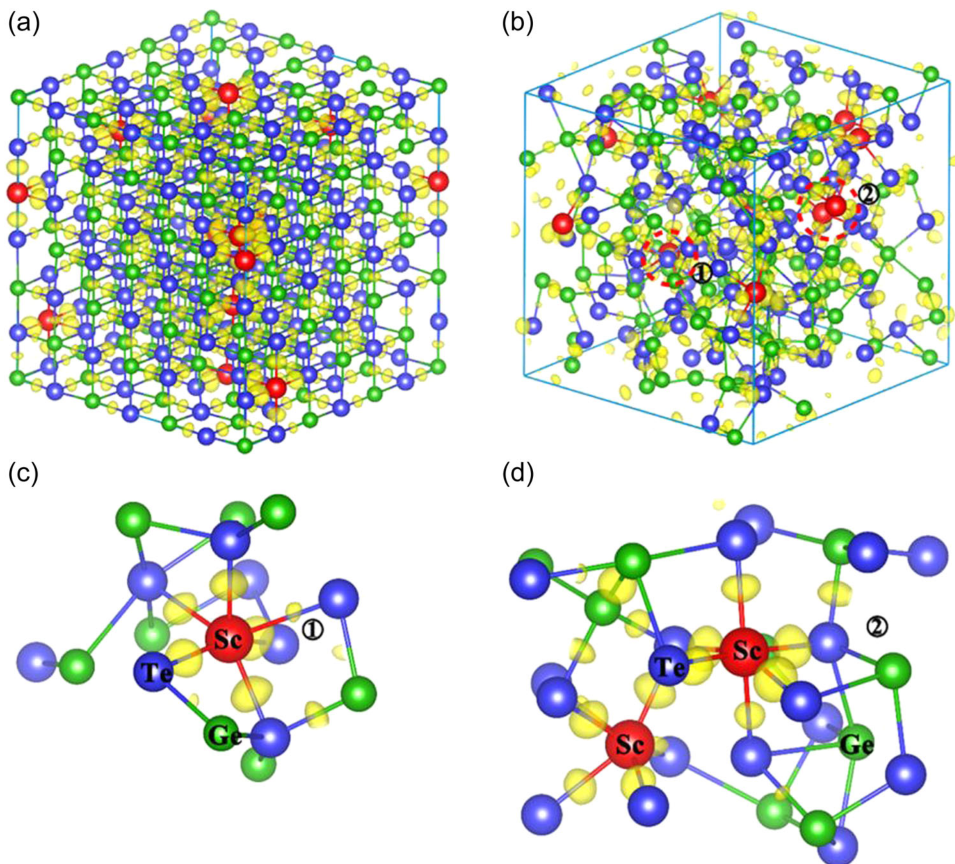

FIGURE 4 Structure models of (a) crystalline and (b) amorphous $Sc_{6.2}Ge_{50}Te_{50}$, with charge density differences used to study the bonding strength; (c, d) typical atomic motifs with charge density differences and bond length values extracted from amorphous $Sc_{6.2}Ge_{50}Te_{50}$ model. The isosurface value is fixed at +0.008e a_0^{-3} (a_0 = Bohr radius). Reprinted with permission from Wang et al. [43] Copyright 2019 American Chemical Society.

An even broader overview is given in Raty et al. [54] Using quantum-topological methods, the authors calculated a two-dimensional map of electronic interaction and bonding in a large range of materials, as depicted in Figure 5 [54]. The Peierls distortion, marked by gray lines in the green "metavalent bonding" area, becomes very large in the amorphous phase of PCMs, which results in a strong difference of electronic and optical properties with respect to the undistorted cubic phase.

SbTe alloys

In the standard $Ge_2Sb_2Te_5$ PCM, the Ge is necessary to avoid recrystallization at relatively low temperatures [55]. Nevertheless, there are some alloys containing Sb-Te that can be used as PCMs, either by addition of other elements, therefore modifying the atomic disorder in the rock salt phase, or by reduction of the system dimensions to the nanoscale. Xu et al. [56] showed by ab initio simulations and transport experiments that Sb_2Te_3 with tailored atomic disorder can have resistance ratios between amorphous and crystalline states of 7 orders of magnitude, allowing for measuring 12 different crystalline states with reliably different resistance

Wang et al. [57] suggested using a monolayer Sb_2Te_3 instead, to reach very fast transition times of below 1 ns. They found that the SET times significantly changed with the substrates/capping layers between which the monolayer was sandwiched, as depicted in Figure 6. Although hexagonal boron nitride enabled SET recrystallization in only 0.12 ns, passivated SiO_2 necessitated 0.54 ns for recrystallization and unpassivated SiO_2 did not allow recrystallization of the monolayer at all.

Doping with Ag was suggested by Hwang et al. [58] to increase the crystallization temperature and reduce the operation energy due to change in the local structure upon Sb substitution by Ag, leading to strong Ag-Te bonds. Doping with yttrium led to $Y_{3.7}Sb_{40.3}Te_{56.0}$, which showed three clearly different states, that is, amorphous, metastable cubic, and stable hexagonal crystalline, and very low power consumption of 0.6–4.3 pJ combined with very low resistance drift and more than 10^6 operation cycles, making this material interesting for PCM applications [59]. Doping with erbium to get $Er_{0.17}Sb_2Te$ resulted in a fast operation speed of 6 ns and 10-year data retention of 121°C, which was attributed

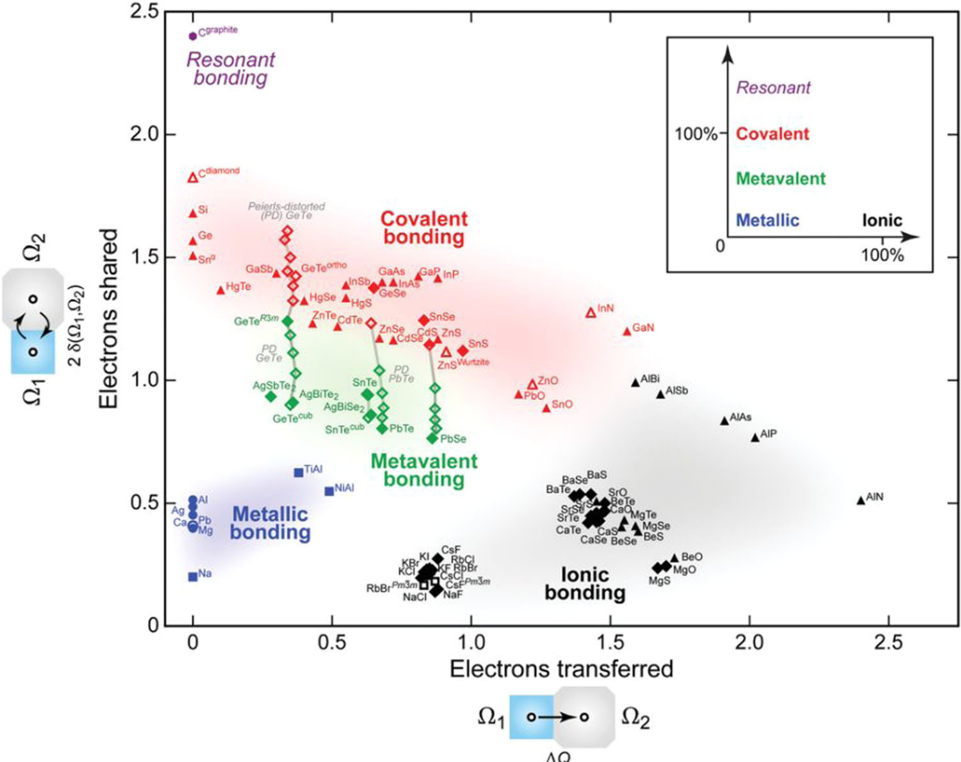

FIGURE 5 Map of electronic interactions and bonding in diverse materials. The symbols define different structure types: tetrahedrally bonded solids (triangles), distorted and ideal rock salt-type (octahedrally coordinated; diamonds), body-centered structures (squares), and close-packed metal structures (circles). Filled symbols correspond to thermodynamically stable phases (at 0 K), while open symbols show metastable phases. For GeTe, SnTe, PbTe, and PbSe, additional structural intermediates have been generated along the Peierls distortion coordinate (gray lines are guides to the eye). From Raty et al. [54], originally published under a CC-BY-NC-ND license.

Substrate/ Superstrate	Structure	SET Speed
BN (weak)		120ps
Passivated SiO_2 (medium)		540ps
Unpassivated SiO_2 (strong)		✗

FIGURE 6 Influence of substrate/superstrate on the recrystallization (SET) of the monolayer Sb_2Te_3. Hexagonal BN, passivated SiO_2, and unpassivated SiO_2 are used as the substrate and/or superstrate, giving rise to different amorphous structures and relative SET times. Color code: Sb (purple), Te (orange), Si (yellow), O (red), H (white), B (green), N (blue). From Wang et al. [57], originally published under a CC-BY license.

to the strong Er-Te bonds, stabilizing glassy states [60]. Similar positive effects were found for other doped Sb-Te alloys, such as Ta-doped Sb_2Te [61], Al-doped Sb_2Te [62], In_3SbTe_2 with an extremely small delay time below 50 ps [63], or $Cu_{0.25}Sb_3Te$ [64].

Besides doping Sb-Te alloys, multilayer $Sb_2Te_3/TiTe_3$ systems were found to enable fast crystallization times of 10 ns and up to 2×10^7 operation cycles [65].

Other Te alloys

Besides the aforementioned alloys, there are a few other Te alloys used for PCM reported in the literature. Rehn et al. [66] suggested monolayer $MoTe_2$ based on density functional theory calculations. They showed that in common $Ge_2Sb_2Te_5$, most of the energy for the thermally driven phase transition is dissipated as heat, whereas the transition in a $MoTe_2$ monolayer is driven electrostatically, leading to a significantly reduced energy consumption as compared with $Ge_2Sb_2Te_5$.

$Er_{13}Te_{87}$ and the Sb-based alloy $Er_{20}Sb_{80}$ showed fast writing speed combined with high data retention, which was again attributed to strong Er-Te and Er-Sb bonds [67], as mentioned before for the ternary alloy $Er_{0.17}Sb_2Te$ [60].

Sb alloys

Some Sb alloys without Te can also be used as PCM materials. For Ge_8Sb_{92}, Wu et al. [68] showed that with decreasing film thickness, the typical PCM properties were improved, that is, crystallization temperature, crystallization energy, and data retention were increased. Using X-ray diffraction, this could be attributed to reduced grain dimensions in thinner films. However, the lower power consumption was accompanied with lower switching speed in thinner films.

Doping $Ge_{10}Sb_{90}$ with Se resulted in increased thermal stability, higher reliability, and decreased operation current, as compared with the base material [69]. For more than 15 at% Se, sheet resistance ratios of more than 10^6 were found, which is higher than typical values of $Ge_2Sb_2Te_5$ films. As a compromise between surface morphology, roughness, and phase transition properties, doping with 8 at% Se was suggested as optimum for PCM materials. Similarly, Ce-doped $Zn_{0.15}Sb_{0.85}$ was found to show significantly improved thermal stability and reduction of the RESET current as compared with pure ZnSb [70]. Besides, superlattice films of $Mg_{35}Sb_{65}/Sn_{15}Sb_{85}$ were prepared by magnetron-sputtering and showed good thermal stability, low power consumption and a fast phase transition [71].

Another interesting candidate for PCM materials is pure antimony. Although films of 10 nm thickness showed only phase change properties at low temperatures of 100 K, reducing the film thickness to 3 nm enabled a significantly increased retention time at room temperature; however, the measured retention time of around 30 s is not comparable to those of typical PCMs [72]. In another approach, the group reported about fast-enough melt quenching the material due to highly trapezoidal voltage pulses to produce a semiconducting state with more than 2.5 orders of magnitude increased resistance, as compared with the fully crystalline state [73].

Other PCM materials

Besides the aforementioned alloys based on Ge, Sb, and/or Te, a few other alloys have been reported in the literature as possible candidates for PCMs. Neumann et al. [74] suggested monolayer MoS_2 [72], similar to the aforementioned monolayer $MoTe_2$ [66]. They found a significantly reduced RESET current in comparison with thicker PCM cells [74]. In $K_2Bi_8Se_{13}$, Islam et al. [75] found a three-dimensional (3D) network of ionic and covalent bonds, leading to a resistance difference by nearly two orders of magnitude and fast crystallization, making this material promising for future PCM.

MULTILEVEL CELL PCM

An interesting property of PCM is that it can have more than just two values. Depending on the programming current used for SET and RESET pulses, some materials allow reaching many intermediate states [76]. Other material systems enable reaching three or even a few more states [77], in this way enabling to store more than 1 bit per cell, as it was also suggested by some research groups dealing with magnetic quaternary or higher-order memory [78–80]. The continuous variation of the resistance with varying programming current is normally applied in non-von Neumann computers, as described in the next section, or can support development of quantum computers. Here we concentrate on systems with few well-defined resistance levels.

A 2 bit system was proposed by Xie et al. [81], who tested different SET operations to gain different resistances, as depicted in Figure 7. Figure 7a depicts the cumulative percentage of resistance for the four different states, showing that they are clearly separated without an overlap. The corresponding ramp-down current pulses, chosen among several variations, are shown in Figure 7b. Another programming scheme, based on reading the cell resistance after each step-by-step increased current pulse, was not further taken into account, as it needs much longer to reach the same states. The authors showed that resistance drift did not lead to an overlap of the states. Their simulations revealed readout times of maximum 65 ns per state.

Song et al. [82] reported on a 12-state PCM system based on carbon-doped $Ge_2Sb_2Te_5$. They describe that carbon in the form of C–C chains and C clusters formed at the $Ge_2Sb_2Te_5$ grain boundaries, resulting in a modification of the grain size and increasing Ge/Sb atomic migration barriers, and thus in an increase of endurance and drift of the PCM chip. Working with a 128 Mb PCM chip, they showed 12 stable levels over 5×10^8 cycles.

Five stable levels were reached by Jin et al. [83] in $GeTe/Sb_2Te_3$ superlattice PCMs by a designed voltage-based pulse. They showed that by varying the voltage pulse height and length, different resistances could be gained with sufficiently low resistance drift. Interestingly, the so-called interfacial PCM based on the superlattice structure necessitated approximately one order of magnitude less energy than common PCMs.

Xu et al. [84] also worked on a superlattice, in this case on a $Sb_7Te_3/GeSb_6Te$ multilayer thin film produced by magnetron sputtering, to reach three different resistance states by applying different voltage pulses. The authors showed that the switching speed reached 40 ns, whereas the resistance drift with time was negligible. In a 2 bit system, that is, based on four different states, the write speed was below 300 ns and thus much slower, but the authors showed for 100 cells a robust operation of more than 10^9 cycles [85].

A more general investigation of the resistance drift over time was performed by Li et al. [86] Combining theoretical calculations with experiments, they suggested that the resistance drift was based on the change of electron binding energy due to structural relaxation, and that it was antiproportional to the dielectric coefficient of the material under investigation. This means that the resistance drift should be reduced by improving the thermal stability of the dielectric coefficient. Based on this assumption, they could approx. bisect the resistance drift by tailoring the samples accordingly.

As these examples show, there are different approaches to produce multilevel PCM cells with varying numbers of levels and

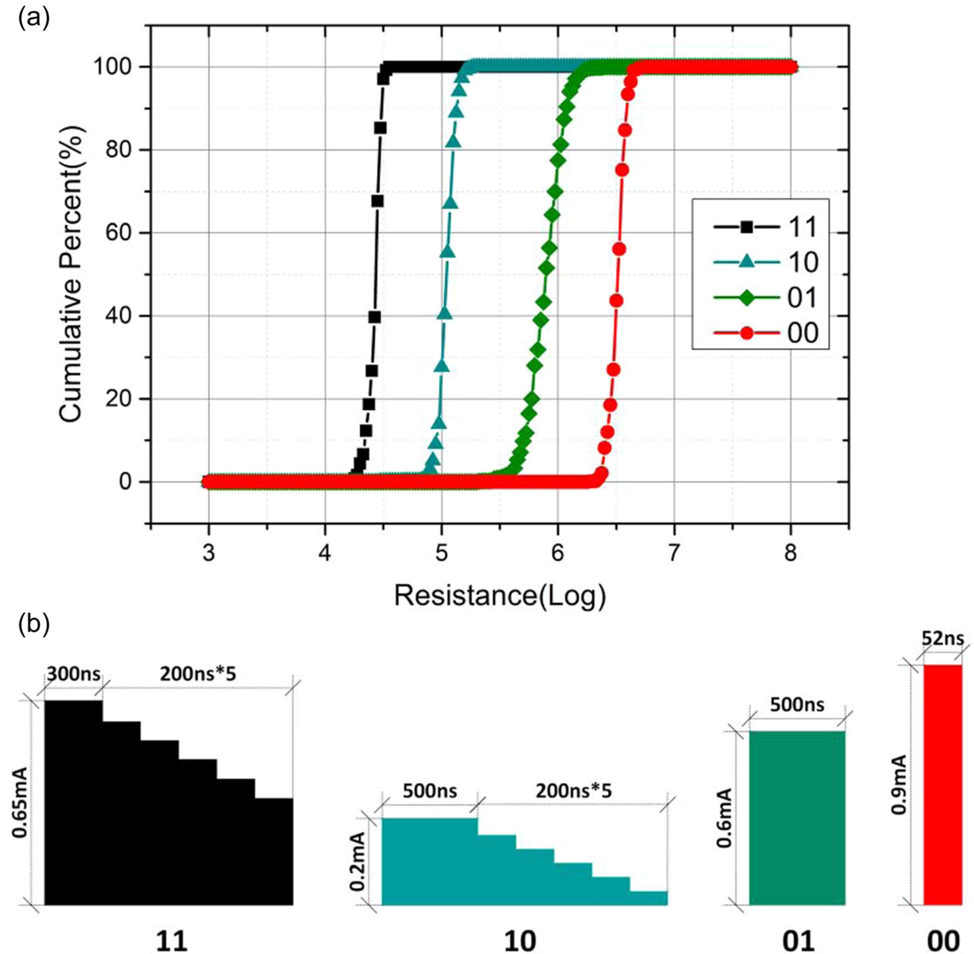

FIGURE 7 (a) Resistance distribution of four states in phase-change memory (PCM) cells; (**b**) the corresponding ramp-down current pulses. From Xie et al. [81], originally published under a CC-BY license.

long-term stability is reached in many research projects. Going one step further, a continuum of levels is taken into account instead of a small number of separate levels, leading to different ideas to used PCMs for non-von Neumann computers, as described in the next section.

PCM FOR NON-VON NEUMANN COMPUTERS

PCM devices are usually applied as an alternative for recent nonvolatile memories. The multilevel approach described in the last section, however, enables using them also as biologically-inspired artificial synapses [87]. The idea behind this approach is that in neuromorphic (cognitive) computing, an accumulation of inputs (i.e., "remembering" the history of the current flowing through it) is used before switching to another state is possible [88–90], typically combined with "forgetting," that is, a reduction of this accumulated input value with time [91–93]. In this way, data storage and processing can be performed at the same position, or an artificial integrate-and-fire neuron can be produced, so that both "neurons" and "synapses" could be based on phase change materials [94,95].

Besides neuromorphic computing, the similar approach of in-memory computing is often mentioned [96]. Here again, the possibility to achieve a broad range of different resistance values is important. Sebastian et al. [97] differentiate between three levels of brain-inspired computing by PCM: first the in-memory computing, that is, coexistence of memory and processing; second as co-processor with multiple PCM cross-bar arrays to speed up training of deep neural networks (DNNs); and third using PCMs as substrates for spiking neural networks (SNNs).

Many studies were published on the possibility to perform in-memory computing by PCM. Giannopoulos et al. [98] showed that the usually problematic precision of such operations could be overcome by so-called projected PCM devices in which temperature-dependent variations of the resistance were compensated using a simple model. They produced PCM devices with 8 bit precision and connected 30 of them to perform image classification by a neural network. The same group used in-memory computing for the fast and robust compressed sensing of sparse signals [99]. Compressed sensing describes approaches to sample and compress

signals at the same time, which necessitates complex algorithms with high memory requirements, making it one of the areas where in-memory computing is expected to reduce memory and computing resources. They showed similar accuracy of the chosen compressed sensing algorithm on their prototype multilevel PCM chip consisting of more than 256 k PCM devices, as compared with fixed-point implementation with matrix and vector elements quantized to 4 bit.

Recently, Khaddam-Aljameh et al. [100,101] reported about a 256 × 256 in-memory core based on the 14 nm technology with multilevel PCM. They combined 256 linearized analog-digital converters based on current controlled oscillators with a local digital processing unit and showed reliable matrix-vector multiplication over 1 GHz, as well as a high classification accuracy when this in-memory computation core was applied for deep learning.

The temperature dependence of such in-memory computing devices based on PCMs was discussed by Boybat et al. [102] They investigated the conductance states for multilevel PCMs in which synaptic weights for deep learning applications were stored by characterization of a large number of 10,000 doped $Ge_2Sb_2Te_5$-based PCMs and modeled the temperature dependence of the conductance states. Interestingly, for different networks such as convolutional neural networks, recurrent neural networks (RNNs), and multilayer perceptron with more than 10^6 PCM weights, they found that a simple array-level scaling was sufficient to correct the temperature-dependent shift of the conductance and restore the accuracy of the networks.

DNNs are usually applied for image and speech detection and are assumed to be helpful for autonomous cars and other future applications. PCM belong to the possible alternatives to recent von Neumann-based computers to speed up processing and reduce the necessary energy [103]. To avoid the inaccuracies of the analog weights programmed in PCM devices, networks can fully be trained on common hardware [104], or the hardware weights can slightly be optimized after a trained model is transferred onto the chip [105]. Joshi et al. [103] investigated the possibility to inject noise during training instead. This noise was estimated from a general hardware characterization, taking into account read and write noise, which led to an experimental accuracy of nearly 94%.

Nandakumar et al. [106] described a possibility to use PCMs as non-von Neumann coprocessors during training of DNNs. In such systems, a dense crossbar array of PCMs is part of the training, with the matrix multiplications performed during forward and backward propagation by Kirchhoff's circuit laws in the crossbar. Programming pulses are used to modify the resistance of the PCMs, that is, to update their weights. The problem of imperfect PCM behavior reducing training accuracy was in this case overcome by a mixed-precision architecture, combining a high-precision digital unit for the weight updates with PCM crossbar arrays for storing the synaptic weights in resistance states. In this way, it was possible to reach high classification accuracy in spite of inaccurate resistance updates.

The conductance drift over time of such systems was investigated by Boybat et al. [107], who used 10,000 PCM devices for their investigation. The group showed that the drift depended on the conductance and could be removed by applying a full or partial SET pulse. In this way, they suggested improving the drift resilience of PCM systems used for training of DNNs. Kariyappa et al. [108] suggested combining drift regularization and multiplicative noise training to improve the noise resiliency of DNNs, based on PCM weight values. They showed that these techniques could improve the model accuracy by 12% during 1 month, working with DNNs for image classification and RNNs for language modeling, respectively.

Combining PCM with dynamic random access memory (DRAM) chips, Lin and Wang [109] investigated the temperature development and the necessary temperature management in 3D DRAM-PCM memory stacks used for DNNs. They developed a memory management which took into account the temperature development, in this way reducing the power and the peak temperature by more than 26 K.

Using in-memory computing PCMs for SNNs belongs to the latest approaches in the application of PCMs. Although SNNs are often built from digital parts, making large static random access memory circuits necessary, in-memory computing could overcome this problem by storing the synaptic weights in the resistance values, enabling parallel real-time processing [110]. Nandakumar et al. [111] reported about an on-chip training investigation based on a prototype chip with more than 10^6 doped $Ge_2Sb_2Te_5$ PCM devices based on the 90 nm node. They used ~180,000 PCMs for supervised training by incremental and stochastic updates to produce spikes at defined times with a precision of a few milliseconds [110].

To enable using advances of artificial neural networks (ANNs), Wozniak et al. [112] suggested combining ANNs and SNNs by a so-called spiking neural unit (SNU), which could be used in both networks. With these SNUs, they received accuracies comparable to ANNs and showed in-memory acceleration during training and inference, based on an in-memory based SNN for music prediction with 52,800 PCM devices.

Pedretti et al. [113] used PCMs as stochastic spiking neurons, where the PCM created noise on which random spikes were based [111]. This stochastic approach, depicted in Figure 8 [113], is used to avoid that the system is trapped within a local minimum, a problem occurring in large Hopfield RNNs solving constraint satisfaction problems such as Sudoku [114]. It means that from synchronous spikes, a stochastic stepwise increase of the internal potential results, leading to a certain randomness of the output spikes. This stochastic behavior is based on the stochastic properties of the crystallization process (Figure 8b). Pedretti et al. [113] showed that their spiking recurrent neural network with stochastic PCM neurons and PCL synapses was able to solve a Sudoku much faster than even recent neuromorphic processors.

Nandakumar et al. [115] reported about a statistical model simulating this cumulative conductance evolution and noise due to reading as well as the temporal conductance drift, comparing spiking and nonspiking ANNs. They used again doped $Ge_2Sb_2Te_5$ to prepare mushroom-type PCM devices produced in the 90 nm node, with 3×10^6 devices on the investigated prototype chip. The model could

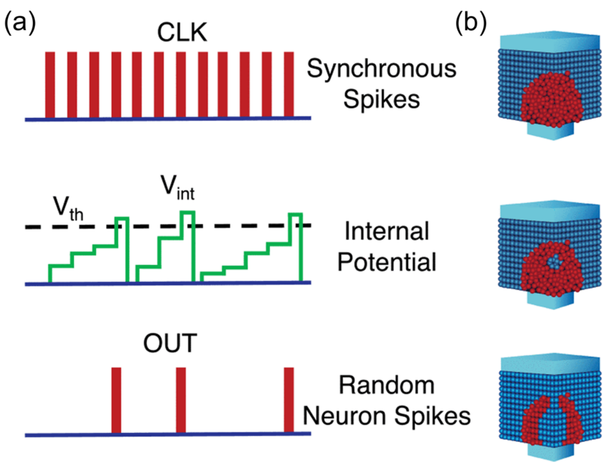

FIGURE 8 (a) Working principle of the proposed stochastic neuron. A sequence of synchronous spikes applied to the neuron leads to a stochastic gradual increase of the internal potential *Vint*. When the threshold *Vth* is reached, a spike is generated, and *Vint* is set to zero. (b) Gradual crystallization process in PCM devices. From Pedretti et al. [113], originally published under a CC-BY license.

be used for the training of ANNs, but was also suggested as a tool to explore diverse neuromorphic algorithms.

To solve the resistivity drift problem, Demirag et al. [116] evaluated the drift behavior of PCMs to enable defining long-term eligibility traces. Oh et al. [117] measured the resistance drift and inserted the results into different neural networks, finding that the resistance drift caused only ~1% of accuracy degradation, whereas the same group found that inserting the measured drift parameters during unsupervised online learning into a SNN for classification of handwritten digits significantly increased the accuracy [118].

On the material side, other challenges are reported. The thickness of PCM films, normally up to some hundred nanometers [119], was significantly reduced to 4 nm by Jiao et al. [120] Using a thin Sb film, they showed the possibility to perform iterative RESET and cumulative SET operations in this system, in which resistance drift and programming noise were low.

In spite of this enormous progress achieved since the first patent dealing with PCM, only few attempts have been made during the last years to commercialize PCMs. These PCMs are described in the next section.

COMMERCIAL PCMS

The first patent suggesting PCM was invented by Ovshinsky [121] before his groundbreaking paper about the possible use of semiconductor phase change materials for data storage and filed by Energy Conversion Devices Inc. Nearly 400 patents cite this one, including many other patents assigned by Energy Conversion Devices Inc., but also by Texas Instruments, Ericsson, IBM, Siemens, Bell Telephone Laboratories Inc. and others, using phase change materials as switches or for PCM approaches. The first commercial PCMs, however, were announced much later.

The first prototype was delivered from Intel and STMicroelectronics in 2008, offering 128 MB memory based on the 90 nm node [122]. This PCRAM was a multilevel cell system with four states [123]. In April 2010, Numonyx and Samsung released their PCRAMs [124,125].

In 2012, Micron launched a 1 Gb PCM based on the 45 nm node, but stopped active selling in 2014 [126]. IBM Intel and Micron launched the Optane™ memory based on the 20 nm node with a data storage density of 0.62 Gb/mm^2, a value which is between commercial NAND products and DRAM products [127]. Although Micron stopped developing the Optane™ technology further in 2021, Intel went on supplying the products [128].

Although DVDs are well-known for a long time now, nonvolatile memories based on phase change materials still face many challenges, such as high programming currents, insufficient data retention, and the necessity of downscaling by incorporating PCMs into smaller and smaller structures, resulting in size effects [129]. All these problems have to be overcome for the development of PCM-based high-density nonvolatile memory.

Recently, the growth in the smartphone market is assumed to accelerate the PCM market growth and areas like automotive and artificial intelligence are expected to further increase the need for PCMs [130]. This underlines the importance to perform further research in this increasing area, enabling better PCMs to be produced.

CONCLUSION

PCM cells are investigated by many research groups, as they are promising alternatives for future nonvolatile memory options. Typical materials are the most often investigated ternary alloy $Ge_2Sb_2Te_5$, as well as various binary and ternary alloys, mostly containing Ge, Sb, and/or Te. Research on the material side concentrates on improving reliability, long-term stability, switching speed and switching current/voltage. On the device side, multilevel cells and implementation in non-von Neumann computers belong to the recent research topics. In spite of the large amount of scientific studies, only few PCM have entered the market since 2008, showing that this technology is not fully mature yet and needs more research and especially transfer into industrialization.

ACKNOWLEDGMENT

Open Access funding enabled and organized by Projekt DEAL.

CONFLICT OF INTEREST

The authors declare no conflict of interest.

DATA AVAILABILITY STATEMENT

Data sharing not applicable to this article, as no data sets were generated or analyzed during the current study.

ORCID

Andrea Ehrmann http://orcid.org/0000-0003-0695-3905
Tomasz Blachowicz http://orcid.org/0000-0002-6569-124X
Guido Ehrmann http://orcid.org/0000-0002-8483-8657
Thomas Grethe http://orcid.org/0000-0001-9625-327X

REFERENCES

[1] S. R. Ovshinsky, *Phys. Rev. Lett.* **1968**, *21*, 1450.
[2] A. Zakery, S. R. Elliott, *J. NonCryst. Solids* **2003**, *330*, 1.
[3] N. Yamada, *Phys. Stat. Sol. B* **2012**, *249*, 1837.
[4] M. Wuttig, N. Yamada, *Nat. Mater.* **2007**, *6*, 824.
[5] A. Lotnyk, M. Behrens, B. Rauschenbach, *Nanoscale Adv.* **2019**, *1*, 3836.
[6] G. W. Burr, M. J. Breitwisch, M. Franceschini, D. Garetto, K. Gopalakrishnan, B. Jackson, B. Kurdi, C. Lam, L. A. Lastras, A. Padilla, B. Rajendran, S. Raoux, R. S. Shenoy, *J. Vacuum Sci. Technol.* **2010**, *28*, 223.
[7] Y. C. Pan, Z. Li, Z. L. Guo, *Crystals* **2019**, *9*, 136.
[8] B.-S. Lee, J. R. Abelson, *J. Appl. Phys.* **2005**, *97*, 093509.
[9] N. Yamada, *J. Appl. Phys.* **2000**, *88*, 7020.
[10] M. Wuttig, V. L. Deringer, X. Gonze, C. Bichara, J.-Y. Raty, *Adv. Mater.* **2018**, *30*, 1803777.
[11] B. J. Kooi, M. Wuttig, *Adv. Mater.* **2020**, *32*, 1908302.
[12] Z. T. Song, R. B. Wang, Y. Xue, S. N. Song, *Nano Res.* **2022**, *15*, 765.
[13] R. O. Jones, *Phys. Rev. B* **2020**, *101*, 024103.
[14] F. C. Mocanu, K. Konstantinou, T. H. Lee, N. Bernstein, V. L. Deringer, G. Csányi, S. R. Elliott, *J. Phys. Chem. B* **2018**, *38*, 8998.
[15] M. Lewis, L. N. Brush, *Nanotechnology* **2022**, *33*, 205204.
[16] N.-K. Chen, X.-B. Li, X.-P. Wang, W. Q. Tian, S. B. Zhang, *Acta Mater.* **2018**, *143*, 102.
[17] V. Adinolfi, L. X. Cheng, M. Laudato, R. C. Clarke, V. K. Narasimhan, S. Balatti, S. Hoang, *ACS Nano* **2019**, *13*, 10440.
[18] P. I. Lazarenko, Y.uV. Vorobyov, M. E. Fedyanina, A. A. Sherchenkov, S. A. Kozyukhin, A. O. Yakubov, A. V. Kukin, Y.uS. Sybina, I. V. Sagunova, *Inorg. Mater. Appl. Res.* **2020**, *11*, 330.
[19] S. Carillo, L. G.-C. Trimby, Y.-Y. Au, V. K. Nagareddy, G. Rodriguez-Hernandez, P. Hosseini, C. Ríos, H. Bhaskaran, C. D. Wright, *Adv. Opt. Mater.* **2019**, *7*, 1801782.
[20] M. Behrens, A. Lotnyk, H. Bryja, J. W. Gerlach, B. Rauschenbach, *Materials* **2020**, *13*, 2082.
[21] S. A. Kozyukhin, *Russ. J. Inorg. Chem.* **2021**, *66*, 281.
[22] S. Vikhrov, P. Nagels, P. Bhat, *Recent Developments in Condensed Matter Physics: Metals, Disordered Systems, Surfaces, and Interfaces*, 2, Plenum, New York **1981**, p. 333.
[23] D. R. Lide *CRC Handbook Chemistry and Physics*, 90th ed. CRC, Boca Raton, FL **2009**.
[24] W. C. Fang, S. N. Song, J. Zhao, C. X. Li, D. L. Cai, Z. T. Song, *Mater. Res. Bulletin* **2022**, *149*, 111731.
[25] Y. J. Chen, N. Chen, B. Chen, Q. Zhang, X. B. Li, Q. S. Deng, B. Zhang, S. B. Zhang, Z. Zhang, X. D. Han, *J. Appl. Phys.* **2018**, *124*, 1451047.
[26] Y. Wang, Y. H. Zheng, G. Y. Liu, T. Li, T. Q. Guo, Y. Cheng, S. L. Lv, S. N. Song, K. Ren, Z. T. Song, *Appl. Phys. Lett.* **2018**, *112*, 133104.
[27] G. X. Wang, Q. H. Nie, X. Shen, R. P. Wang, L. C. Wu, J. Fu, T. F. Xu, S. X. Dai, *Appl. Phys. Lett.* **2012**, *101*, 051906.
[28] R. B. Wang, Z. T. Song, W. X. Song, T. J. Xin, S. Lv, S. Song, *InfoMat* **2021**, *3*, 1008.
[29] S. M. S. Privitera, I. López García, C. Gongiorno, V. Sousa, M. C. Cyrille, G. Navarro, C. Sabbione, E. Carria, *J. Appl. Phys.* **2020**, *128*, 155105.
[30] A. Kusiak, C. Chassain, A. M. Canseco, K. Ghosh, M.-C. Cyrille, A. L. Serra, G. Navarro, M. Bernard, N.-P. Tran, J.-L. Battaglia, *Phys. Stat. Solid. RRL* **2022**, *16*, 2100507.
[31] S. Cecchi, I. Lopez Garcia, A. M. Mio, E. Zallo, O. A. El Kheir, R. Calarco, M. Bernasconi, G. Nicotra, S. M. S. Privitera, *Nanomaterials* **2022**, *12*, 631.
[32] O. A. El Kheir, D. Dragoni, M. Bernasconi, *Phys. Rev. Mater.* **2021**, *5*, 095004.
[33] M. Boniardi, J. E. Boschker, J. Momand, B. J. Kooi, A. Redaelli, R. Calarco, *Phys. Stat. Sol. RRL* **2019**, *13*, 1800634.
[34] Y. Cheng, D. L. Cai, Y. H. Zheng, S. Yan, L. Wu, C. Li, W. X. Song, T. J. Xin, S. L. Lv, R. Huang, H. B. Lv, Z. T. Song, S. L. Feng, *ACS Appl. Mater. Interfaces* **2020**, *12*, 23051.
[35] J. H. Han, H. Jeong, H. J. Park, H. D. Kwon, D. S. Kim, D. H. Lim, S. J. Baik, Y.-K. Kwon, M.-H. Cho, *RSC Adv.* **2021**, *11*, 22479.
[36] X. Li, H. P. Chen, C. C. Xie, D. L. Cai, S. N. Song, Y. F. Chen, Y. Lei, M. Zhu, *Phys. Stat. Sol. RRL* **2019**, *13*, 1088558.
[37] Z. T. Song, D. L. Cai, X. Li, L. Wang, Y. F. Chen, H. P. Chen, Q. Wang, Y. P. Zhan, M. H. Ji, **2018**, *IEEE Int. Electron Devices Meet. (IEDM)* 27.5.1–27.5.4.
[38] M. A. Luong, N. Cherkashin, B. Pecassou, C. Sabbione, F. Mazen, A. Claverie, *Nanomaterials* **2021**, *11*, 1729.
[39] X. Yu, Y. Zhao, C. Li, C. Q. Hu, L. Ma, S. H. Fan, Y. Zhao, N. Min, S. P. Tao, Y. L. Wang, *Script. Mater.*, **2017**, *141*, pp. 120.
[40] M. A. Luong, D. F. Wen, E. Rahier, N. R. Ramond, B. Pecassou, Y. Le Friec, D. Benoit, A. Claverie, *Phys. Stat. Solid. RRL* **2021**, *15*, 2000443.
[41] M. Zhu, K. Ren, L. Liu, S. L. Lv, X. S. Miao, M. Xu, Z. T. Song, *Phys. Rev. Mater.* **2019**, *3*, 033603.
[42] T. Blachowicz, M. G. Beghi, G. Güntherodt, B. Beschoten, H. Dieker, *J. Appl. Phys.* **2007**, *102*, 093519.
[43] Y. Wang, T. Q. Guo, G. Y. Liu, T. Li, S. L. Lv, S. N. Song, Y. Cheng, W. X. Song, K. Ren, Z. T. Song, *ACS Appl. Mater. Interfaces* **2019**, *11*, 10848.
[44] Y. Saito, S. Hatayama, Y. Shuang, S. Shindo, P. Fons, A. V. Kolobov, K. Kobayashi, Y. Sutou, *Appl. Phys. Express* **2019**, *12*, 051008.
[45] Y. H. Chen, L. Sun, Y. X. Zhou, T. M. Zewdie, V. L. Deringer, R. Mazzarello, W. Zhang, *J. Mater. Chem. C* **2020**, *8*, 71.
[46] A. N. D. Kolb, N. Bernier, E. Robin, A. Benayad, J.-L. Rouvière, C. Sabbione, F. Hippert, P. Noé, *ACS Appl. Electron. Mater* **2019**, *1*, 701.
[47] G. Modi, E. A. Stach, *ACS Nano* **2020**, *14*, 2162.
[48] Y. Saito, P. Fons, A. V. Kolobov, K. V. Mitrofanov, K. Makino, J. Tominaga, S. Hatayama, Y. Sutou, M. Hase, J. Robertson, *J. Phys. D. Appl. Phys.* **2020**, *53*, 284002.
[49] Y. Shuang, Y. Sutou, S. Hatayama, S. Shindo, Y. H. Song, D. Ando, J. Koike, *Appl. Phys. Lett.* **2018**, *112*, 183504.
[50] S. Shindo, Y. Shuang, S. Hatayama, Y. Saito, P. Fons, A. V. Kolobov, K. Kobayashi, Y. Sutou, *J. Appl. Phys.* **2020**, *128*, 162105.
[51] Z. G. Li, Y. G. Lu, M. Wang, X. Shen, X. H. Zhang, S. N. Song, Z. T. Song, *J. Noncryst. Solids* **2018**, *481*, 110.
[52] K. L. Okabe, A. Sood, E. Yalon, C. M. Neumann, M. Asheghi, E. Pop, K. E. Goodson, H.-S.P. Wong, *J. Appl. Phys.* **2019**, *125*, 184501.
[53] C. Persch, M. J. Müller, A. Yadav, J. Pries, N. Honné, P. Kerres, S. Wei, H. Tanaka, P. Fantini, E. Varesi, F. Pellizzer, M. Wuttig, *Nat. Commun.* **2021**, *12*, 4978.
[54] J.-Y. Raty, M. Schumacher, P. Golub, V. L. Deringer, C. Gatti, M. Wuttig, *Adv. Mater.* **2018**, *31*, 1806280.
[55] P. Arun, P. Tyagi, A. G. Vedeshwar, V. K. Paliwal, *Phys. B Cond. Matter* **2001**, *307*, 105.
[56] Y. Xu, X. Wang, W. Zhang, L. Schäfer, J. Reindl, F. vom Bruch, Y. Zhou, V. Evang, J. Wang, V. L. Deringer, E. Ma, M. Wuttig, R. Mazzarello, *Adv. Mater.* **2021**, *33*, 2006221.
[57] X.-P. Wang, X.-B. Li, N.-K. Chen, B. Chen, F. Rao, S. B. Zhang, *Adv. Sci.* **2021**, *8*, 2004185.

[58] S. B. Hwang, H. J. Park, D. S. Kim, H. W. Lim, C. W. Lee, J. H. Han, Y.-K. Kwon, *ACS Appl. Mater. Interfaces* **2020**, *12*, 37285.
[59] B. Liu, K. Q. Li, W. L. Liu, J. Zhou, L. C. Wu, Z. T. Song, S. R. Elliott, Z. M. Sun, *Sci. Bull*. **2021**, *66*, 2217.
[60] J. Zhao, Z. H. Yuan, W.-X. Song, Z. T. Song, *J. Alloys Compd*. **2021**, *889*, 161701.
[61] Y. Xue, S. Yan, S. L. Lv, S. N. Song, Z. T. Song, *Nanomicro Lett*. **2021**, *13*, 33.
[62] Y. Wang, T. B. Wang, Y. H. Zheng, G. Y. Liu, T. Li, S. L. Lv, W. X. Song, S. N. Song, Y. Cheng, K. R. Z. T., Song, *Sci. Rep*. **2018**, *8*, 15136.
[63] N. Saxena, C. Persch, M. Wuttig, *Sci. Rep*. **2019**, *9*, 19251.
[64] S. Yan, D. L. Cai, Y. Xue, T. Q. Guo, S. N. Song, Z. T. Song, *Mater. Sci. Semicond. Process*. **2019**, *103*, 104625.
[65] J. B. Shen, S. L. Lv, X. Chen, T. Li, S. F. Zhang, Z. T. Song, M. Zhu, *ACS Appl. Mater. Interfaces* **2019**, *11*, 5336.
[66] D. A. Rehn, Y. li, E. Pop, E. J. Reed, *NPJ Comput. Mater*. **2018**, *4*, 2.
[67] J. Zhao, Z. H. Yuan, X. D. Li, W.-X. Song, Z. T. Song, *J. Alloys Comp*. **2022**, *904*, 164057.
[68] W. H. Wu, Z. H. Zhao, B. Shen, J. W. Zhai, S. N. Song, Z. T. Song, *Nanoscale* **2018**, *10*, 7228.
[69] J. H. Kim, J. H. Park, D.-H. Ko, *Thin Solid Films* **2018**, *653*, 173.
[70] H. Zou, L. J. Zhai, Y. F. Hu, J. H. Zhang, X. Q. Zhu, Y. M. Sun, Z. T. Song, *Appl. Phys. A: Mater. Sci. Process*. **2018**, *124*, 717.
[71] S. Sun, Y. F. Hu, T. S. Lai, X. Q. Zhu, *J. Mater. Sci. Mater. Electron*. **2020**, *31*, 12476.
[72] B. Kersting, M. Salinga, *Faraday Discuss*. **2019**, *213*, 357.
[73] M. Salinga, B. Kersting, I. Ronneberger, V. P. Jonnalagadda, X. T. Vu, M. Le Gallo, I. Giannopoulos, O. Cojocaru-Mirédin, R. Mazzarello, A. Sebastian, *Nat. Mater*. **2018**, *17*, 681.
[74] C. M. Neumann, K. L. Okabe, E. Yalon, R. W. Grady, H.-S.P. Wong, E. Pop, *Appl. Phys. Lett*. **2019**, *114*, 082103.
[75] S. M. Islam, V. K. Sangwan, D. Bruce Buchholz, S. A. Wells, L. Peng, L. Zeng, Y. He, M. C. Hersam, J. B. Ketterson, T. J. Marks, M. J. Bedzyk, M. Grayson, M. G. Kanatzidis, *J. Am. Chem. Soc*. **2021**, *143*, 6221.
[76] N. Papandreou, A. Pantazi, A. Sebastian, E. Eleftheriou, M. Breitwisch, C. Lam, *Solid State Electron*. **2010**, *54*, 991.
[77] L. Zheng, W. X. Song, Z. T. Song, S. S, *ACS Appl. Mater. Interfaces* **2019**, *11*, 45885.
[78] D. Sudsom, A. Ehrmann, *Nanomaterials* **2021**, *11*, 349.
[79] T. Blachowicz, D. Kosmalska, C. Döpke, H. Leiste, L. Hahn, *J. Magn. Magn. Mater*. **2019**, *491*, 165619.
[80] T. Blachowicz, C. Döpke, A. Ehrmann, *Nanomaterials* **2020**, *10*, 738.
[81] C. C. Xie, X. Li, H. P. Chen, Y. Li, Y. G. Liu, Q. Wang, K. Ren, Z. T. Song, *Micromachines* **2019**, *10*, 461.
[82] Z. T. Song, D. L. Cai, Y. Cheng, L. Wang, S. L. Lv, T. J. Xin, G. M. Feng, *Nanoscale* **2021**, *23*, 10445.
[83] S.-M. Jin, S.-Y. Kang, H.-J. Kim, J.u-Y. Lee, I. H. Nam, T.-H. Shim, Y.-H. Song, J.-G. Park, *Electron. Lett*. **2022**, *58*, 38.
[84] Z. H. Xu, X. Su, S. C. Hua, J. W. Zhai, S. Song, Z. T. Song, *Nanotechnology* **2022**, *33*, 075701.
[85] N. Gong, W. Chien, Y. Chou, C. Yeh, N. Li, H. Cheng, C. Cheng, I. Kuo, C. Yang, R. Bruce, A. Ray, L. Gignac, Y. Lin, C. Miller, T. Perri, W. Kim, L. Buzi, H. Utomo, F. Carta, E. Lai, H. Ho, H. Lung, M. BrightSky, *IEEE Symp. VLSI Tech*. **2020**, 1.
[86] C. Li, C. Q. Hu, J. B. Wang, X. Yu, Z. B. Yang, J. Liu, Y. K. Li, C. B. Bi, X. L. Zhou, W. T. Zheng, *J. Mater. Chem. C* **2018**, *6*, 3387.
[87] T. Blachowicz, A. Ehrmann, *Molecules* **2020**, *25*, 2550.
[88] K. M. Song, J.-S. Jeong, B. Pan, X. Zhang, J. Xia, S. Cha, T.-E. Park, K. Kim, S. Finizio, J. Raabe, J. Chang, Y. Zhou, W. Zhao, W. Kang, H. Ju, S. Woo, *Nat. Electron*. **2020**, *3*, 148.
[89] D. Markovic, A. Mizrahi, D. Querlioz, J. Grollier, *Nat. Rev. Phys*. **2020**, *2*, 499.
[90] K.-U. Demasius, A. Kirschen, S. Parkin, *Nat. Electron*. **2021**, *4*, 748.
[91] Y. Wang, L. Yin, W. Huang, Y. Y. Li, S. J. Huang, Y. Y. Zhu, D. Yang, X. D. Pi, *Adv. Intell. Syst*. **2021**, *3*, 2000099.
[92] R. A. John, J. K, M. R. Kulkarni, N. Tiwari, N. A. Chien, N. G. Ing, W. L. Leong, N. Mathews, *Small* **2017**, *13*, 1701193.
[93] T. Blachowicz, J. Grzybowski, P. Steblinski, A. Ehrmann, *Biomimetics* **2021**, *6*, 32.
[94] C. D. Wright, P. Hosseini, J. A. V. Diosdado, *Adv. Funct. Mater*. **2013**, *23*, 2248.
[95] M. Le Gallo, A. Sebastian, *J. Phys. D. Appl. Phys*. **2020**, *53*, 213002.
[96] A. Sebastian, M. Le Gallo, E. Eleftheriou, *J. Phys. D. Appl. Phys*. **2019**, *52*, 443002.
[97] A. Sebastian, M. Le Gallo, G. W. Burr, S. B. Kim, M. BrightSky, E. Eleftheriou, *J. Appl. Phys*. **2018**, *124*, 111101.
[98] I. Giannopoulos, A. Sebastian, M. Le Gallo, V. P. Jonnalagadda, M. Sousa, M. N. Boon, E. Eleftheriou, **2018**, *IEEE Int. Electron Devices Meet. (IEDM)* 27.7.1–27.7.4.
[99] M. Le Gallo, A. Sebastian, G. Cherubini, H. Giefers, *IEEE Trans. Electron Devices* **2018**, *65*, 4304.
[100] R. Khaddam-Aljameh, M. Stanisavljevic, J. Fornt Mas, G. Karunaratne, M. Braendli, F. Liu, A. Singh, S. M. Muller, U. Egger, A. Petropoulos, T. Antonakopoulos, K. Brew, S. Choi, I. K. Ok, F. L. Lie, N. Saulnier, V. Chan, I. Ahsan, V. Narayanan, S. R. Nandakumar, M. Le Gallo, P. A. Francese, A. Sebastian, E. Eleftheriou, **2021**, *Symp. VLSI Circ*. 1–2.
[101] R. Khaddam-Aljameh, M. Stanisavljevic, J. Fornt Mas, G. Karunaratne, M. Brandli, F. Liu, A. Singh, S. M. Muller, U. Egger, A. Petropoulos, T. Antonakopoulos, K. Brew, S. Choi, I. Ok, F. L. Lie, N. Saulnier, V. Chan, I. Ahsan, V. Narayanan, S. R. Nandakumar, M. Le Gallo, P. A. Francese, A. Sebastian, E. Eleftheriou, *IEEE J. Solid State Circ*., **2022**, *57*, 1027. https://doi.org/10.1109/JSSC.2022.3140414
[102] I. Boybat, B. Kersting, S. Ghazi Sarwat, X. Timoneda, R. L. Bruce, M. BrightSky, M. Le Gallo, A. Sebastian, **2021**, *IEEE Int. Electron Devices Meet. (IEDM)* 28.3.1–28.3.4.
[103] V. Joshi, M. Le Gallo, S. Haefeli, I. Boybat, S. R. Nandakumar, C. Piveteau, M. Dazzi, B. Rajendran, A. Sebastian, E. Eleftheriou, *Nat. Commun*. **2020**, *11*, 2473.
[104] S. Ambrogio, P. Narayanan, H. Tsai, R. M. Shelby, I. Boybat, C. di Nolfo, S. Sidler, M. Giordano, M. Bodini, N. Farinha, B. Killeen, C. Cheng, Y. Jaoudi, G. W. Burr, *Nature* **2018**, *558*, 60.
[105] S. K. Gonugondla, M. Kang, N. R. Shanbhag, *IEEE J. Solid State Circuits* **2018**, *53*, 3163.
[106] S. R. Nandakumar, M. Le Gallo, I. Boybat, B. Rajendran, A. Sebastian, E. Eleftheriou, *IEEE Int. Symp. Circ. Syst. (ISCAS)* **2018**, *208*, 1–5.
[107] I. Boybat, S. R. Nandakumar, M. Le Gallo, B. Rajendran, Y. Leblebici, A. Sebastian, E. Eleftheriou, **2018**, *Non-Volatile Memory Technol. Symp. (NVMTS)* 1–4.
[108] S. Kariyappa, H. Tsai, K. Spoon, S. Ambrogio, P. Narayanan, C. Mackin, A. Chen, M. Qureshi, *IEEE Trans. Electron Devices* **2021**, *68*, 4356.
[109] S.-Y. Lin, S.-C. Wang, *Microproc. Microsyst*. **2022**, *89*, 104444.
[110] S. R. Nandakumar, I. Boybat, M. Le Gallo, E. Eleftheriou, A. Sebastian, B. Rajendran, *Sci. Rep*. **2020**, *10*, 8080.
[111] G. F. Close, U. Frey, M. Breitwisch, H. L. Lung, C. Lam, C. Hagleitner, E. Eleftheriou, **2010**, *Int. Electron Devices Meet. 2010* 29.5.1–29.5.4.
[112] S. Wozniak, A. Pantazi, T. Bohnstingl, E. Eleftheriou, *Nat. Machine Intell*. **2020**, *2*, 325.
[113] G. Pedretti, P. Mannocci, S. Hashemkhani, V. Milo, O. Melnic, E. Chicca, *IEEE J. Explor. Solid State Comput. Devices Circ*. **2020**, *6*, 89.
[114] V. Pavlovic, D. Schonfeld, G. Friedman**2001**, *Proc. Neural Netw. Signal Process. XI: IEEE Signal Process. Soc. Workshop* 173–182.

[115] S. R. Nandakumar, M. Le Gallo, I. Boybat, B. Rajendran, A. Sebastian, *J. Appl. Phys*. **2018**, *124*, 152135.

[116] Y. Demirag, F. Moro, T. Dalgaty, G. Navarro, C. Frenkel, G. Indiveri, E. Vianello**2021**, *IEEE Int. Symp. Circ. Syst. (ISCAS)* 1–5.

[117] S. H. Oh, Z. S. Huang, Y. H. Shi, D. Kuzum, *IEEE Electron Device Lett*. **2019**, *40*, 1325.

[118] S. H. Oh, Y. H. Shi, X. Liu, J. W. Song, D. Kuzum, *IEEE Electron Device Lett*. **2018**, *39*, 1768.

[119] I. Boybat, M. Le Gallo, S. R. Nandakumar, T. Moraitis, T. Parnell, T. Tuma, B. Rajendran, Y. Leblebici, A. Sebastian, E. Eleftheriou, *Nat. Commun*. **2018**, *9*, 2514.

[120] F. Y. Jiao, B. Chen, K. Y. Ding, K. L. Li, L. Wang, X. R. Zeng, F. Rao, *Appl. Mater. Today* **2020**, *20*, 100641.

[121] S. R. OvshinskySymmetrical current controlling device. *US3271591A* **1966**

[122] Intel ST. **2022**, https://phys.org/news/2008-02-intel-stmicroelectronics-industry-phase-memory.html (accessed: 12 March 2022).

[123] K. Greene, **2022**, https://www.technologyreview.com/2008/02/04/35301/a-memory-breakthrough (accessed: 12 March 2022).

[124] web.archive.org/web/20100425035721/numonyx.com/en-US/About/PressRoom/Releases/Pages/NewPCMDevices.aspx (accessed: 12 March 2022).

[125] Samsung Ships Industry's First Multi-chip Package with a PRAM Chip for Handsets **2022**, 20100821115849/samsung.com/us/aboutsamsung/news/newsIrRead.do?news_ctgry=irnewsrelease%26page=1%26news_seq=18828%26rdoPeriod=ALL%26from_dt=%26to_dt=%26search_keyword= (accessed: 12 March 2022).

[126] P. Clarke, *Memory – for Now* **2022**, *7*, 2014. https://electronics360.globalspec.com/article/3931/exclusive-micron-drops-phase-change-memory-for-now (accessed: 12 March 2022).

[127] J. D. Cho **2022** https://www.techinsights.com/blog/intel-3d-xpoint-memory-die-removed-intel-optanetm-pcm-phase-change-memory (accessed: 12 March 2022).

[128] C. Sliw **2022** https://www.techtarget.com/searchstorage/news/252499716/Intel-breaks-silence-on-effects-of-Microns-3D-XPoint-exit (accessed: 12 March 2022).

[129] P. Noé, C. Vallée, F. Hippert, F. Fillot, J.-Y. Raty, *Semicond. Sci. Technol*. **2018**, *33*, 013002.

[130] Worldwide Phase Change Memory Industry to 2026 – by Technology, Application and Geography https://www.prnewswire.com/news-releases/worldwide-phase-change-memory-industry-to-2026—by-technology-application-and-geography-301272813.html (accessed: 12 March 2022).

How to cite this article: A. Ehrmann, T. Blachowicz, G. Ehrmann, T. Grethe, *Appl. Res*. **2022**, e202200024. https://doi.org/10.1002/appl.202200024